Wavelet-based adaptive wall-modeled large eddy simulation method for compressible turbulent flows

Xuan Ge,[1,*] Oleg V. Vasilyev,[2,3,†] and M. Yousuff Hussaini[4]
[1]*Convergent Science Incorporated, Madison, Wisconsin 53719, USA*
[2]*Keldysh Institute of Applied Mathematics of Russian Academy of Sciences, Moscow 125047, Russia*
[3]*Adaptive Wavelet Technologies, LLC, Superior, Colorado 80027, USA*
[4]*Florida State University, Tallahassee, Florida 32306, USA*

(Received 12 January 2021; accepted 9 August 2021; published 14 September 2021)

A wavelet-based adaptive wall-modeled large eddy simulation (WA-WMLES) method is proposed for simulations of wall-bounded compressible turbulent flows. The approach utilizes the wavelet-based adaptive large eddy simulation (WA-LES), incorporated into the anisotropic-adaptive wavelet collocation method, to resolve the outer region of turbulent boundary layer, while the inner part is approximated by the equilibrium wall-shear-stress model. Such an approach for modeling the inner layer is crucial for wavelet-based adaptive turbulent flow simulations because the mesh resolution requirement for WA-LES to resolve inner viscous sublayer becomes computationally prohibitively expensive as the Reynolds number increases. In the outer layer region WA-LES computations take advantage of the wavelet-based local mesh refinement, which not only efficiently captures the physical characteristics of flows on a nearly optimal adaptive computational mesh, e.g., massive boundary layer separation, but also actively controls the error of the solution using *a priori* defined wavelet filtering threshold. A flat plate turbulent boundary layer flow and a separated flow over NASA's wall-mounted hump are tested to verify and validate the WA-WMLES approach. Good agreement of the results predicted by the WA-WMLES method is achieved compared to the reference data from experiments and simulations. The finest effective mesh resolution of the WA-WMLES is consistently higher than the one used in the wall-modeled LES (WMLES) found in literature, but comparable to the wall-resolved LES, while the similar accuracy is achieved with considerably fewer degrees of freedom than in nonadaptive WMLES. These observations demonstrate both accuracy and efficiency of the WA-WMLES method.

DOI: 10.1103/PhysRevFluids.6.094606

I. INTRODUCTION

The recent advancements in wavelet-based numerical methodologies to solve partial differential equations, combined with the unique properties of wavelet analysis to unambiguously identify and isolate localized dynamically dominant flow structures, allow the development of a hierarchical adaptive eddy-capturing framework for turbulent flow simulation that fully captures spatial and temporal turbulent flow intermittency and tightly integrates numerics and physics-based modeling [1,2]. In the wavelet simulation, coherent flow structures are either totally or partially resolved on dynamically adaptive computational meshes, while the effect of unresolved motions are represented by the models. The separation between resolved (more energetic) eddies and residual (less energetic)

*Present address: Florida State University, Tallahassee, FL 32306.
†Oleg.V.Vasilyev@AdaptiveWaveletTechnologies.com, Oleg.V.Vasilyev@gmail.com

components of the flow is achieved by means of the nonlinear wavelet thresholding filter. The value of wavelet threshold controls the relative importance of resolved field and residual background flow and, thus, the fidelity of turbulence simulations.

In the wavelet-based adaptive large eddy simulation (WA-LES), the stochastic and the least energetic coherent parts of the turbulent velocity field are discarded and only the most energetic coherent vortices are captured in the resolved numerical solution [3]. It is found in Ref. [4] that the discarded subgrid-scale (SGS) coherent structures dominate the total SGS dissipation, while the SGS incoherent modes have a negligible effect upon the large-scale dynamics and the energy transfer. Therefore, similar to conventional LES methods, many standard LES closures are applicable for the Adaptive LES method by modeling SGS coherent structures in terms of the resolved energetic coherent vortices.

The effectiveness and efficiency of the wavelet-based adaptive wall-resolved LES (WA-WRLES) method has been scrutinized for wall-bounded incompressible or compressible flows using either the volume-penalization boundary condition [2,5] or body-fitted curvilinear meshes [6]. For wall-bounded flows, the anisotropic-adaptive wavelet collocation method (A-AWCM) [7] with body-fitted meshes allows anisotropic mesh clustering and stretching in the physical domain, and, thus, overcomes the difficulty in simulating the flow over complex geometries by traditional wavelet-based methods [8–11] while preserving the efficiency and error control of wavelet transform and mesh adaptation procedure over the uniform meshes in the computational domain.

Despite significant savings achieved by wavelet compression in the WA-WRLES, its application is still computationally prohibitively expensive for high Reynolds number wall-bounded flows. This is a wide and lasting issue for all the efforts in the wall-resolved LES community and is mainly due to progressive decrease of the viscous length scales in the inner region of a turbulent boundary layer requiring very fine wall-normal mesh spacing Δy that scales with Reynolds number as $\Delta y \sim x\mathrm{Re}_x^{-13/14}$ [12]. In contrast, energy-containing length scales in the outer-region are usually determined by the geometry of the flow or more precisely the boundary layer thickness δ, which decreases slowly with the Reynolds number and scales as $\delta \sim x\mathrm{Re}_x^{-1/7}$. In fact, as estimated by Choi and Moin [12], the mesh resolution for the wall-resolved LES approach scales as $N_{\mathrm{wr}} \sim \mathrm{Re}^{13/7}$. Alternatively, the wall-modeled LES [13,14] requires the mesh resolution scaling as $N_{\mathrm{wm}} \sim \mathrm{Re}$. Therefore, the wall-modeled LES is more applicable to high Reynolds number problems, despite some side-effects, such as the log-layer mismatch (LLM) with the error in skin friction of about 5% to 15% [15–17], which is observed when the near-wall RANS model and the resolved LES away from the wall do not quite match their interception constants, C (in $U^+ = \log(y^+)/\kappa + C$) in the log-law layers.

There are two well-known categories of wall-modeled LES methods: (1) the hybrid large eddy simulation and Reynolds-averaged Navier-Stokes (LES-RANS) methods that switch to the RANS formulations in the inner layer [16–19] and (2) the wall-shear-stress methods that model the wall shear stress directly on the wall [20–23]. Recently a wavelet-based adaptive delayed detached eddy simulation (WA-DDES) [24,25] that incorporates hybrid LES-RANS modeling framework into the wavelet-based adaptive unsteady RANS (WA-URANS) [26,27] formulation has been proposed. The developed WA-DDES resolves the typical log-layer mismatch issue encountered in the conventional nonadaptive DDES methods mainly due to the use of wavelet-based adaptive mesh refinement and have been examined in a variety of wall-bounded flow configurations. WA-DDES achieves high grid compression relative to the effective mesh resolution at the highest level while obtaining accurate solutions using relatively small wavelet filtering threshold, especially in the wall modeling RANS region.

One major issue in the WA-DDES computations is the stringent restriction on step size for time integration caused by very small wall-normal mesh spacings immediately adjacent to the wall, i.e., $y^+ < 1$, despite the use of stretched meshes with relatively large parallel grid spacings to reduce the total number of active nodes. The main objective of this work is to overcome this restriction by developing the wavelet-based adaptive wall-modeled LES (WA-WMLES) method. For the rest of context, the term "wall-modeled LES" is used for simplicity to refer to the aforementioned

wall-shear-stress-modeled LES method. The key idea of the WMLES approach is to feed the information to a RANS model at an exchange location (EL) from the LES flow field and then solve the RANS equations (either ordinary differential equations (ODEs) for the equilibrium model [15,28,29] or partial differential equations (PDEs) with 3D RANS computations for the nonequilibrium model [22,23]). The RANS equations are then solved to find the wall stresses (viscous fluxes) to impose the wall-stress boundary conditions back to the LES computation under the assumption that the direction of the wall shear is aligned with the velocity vector at the EL. The EL is a user-defined parameter and can be adjusted based on the boundary layer thickness. To prevent the log-layer mismatch it was recommended in Ref. [15] that the exchange locations should be located in the lower portion of the log-layer and within 10% of the boundary layer thickness, which highlights one of the advantages of the WA-WMLES, namely, the removal of CFL restriction due to near-wall mesh spacing as the first mesh point away from the wall is located above $y^+ \gtrsim 40$. As a result, considerably cheaper explicit time integration schemes can be used in the WA-WMLES computations. It is important to emphasize that the adaptive wavelet-based methodology [8–11] is capable to achieve not only sparse data representation and high grid compression using the inherent adaptive mesh refinement capabilities, but also to control the accuracy of the simulations through wavelet filtering threshold, which is very important for simulation of unsteady turbulent flows with boundary layer separation that can be captured by spatiotemporally adaptive meshes with nearly optimal number of degrees of freedom.

The rest of the paper is organized as follows. Section II introduces the WA-WMLES governing equations, including the Favre-filtered Navier-Stokes equations for compressible flows, the SGS eddy viscosity model and the wall-modeled LES boundary conditions. The A-AWCM and the implementation of the WA-WMLES into the A-AWCM framework are described in Sec. III. Section IV presents the simulation results for the test cases using the WA-WMLES method. Concluding remarks are given in Sec. V.

II. GOVERNING EQUATIONS

A. Favre-filtered Navier-Stokes equations

For conventional nonadaptive LES, the implicit or explicit linear lowpass filtering operator is usually defined a priori and is tied to the corresponding computational mesh with under-resolved mesh spacings relative to DNS. In contrast to standard LES, the wavelet-filtering operator used in the wavelet-based Adaptive LES is constructed by using the wavelet thresholding filter, described in Sec. III, which is nonlinear and depends on the instantaneous flow realization. Similarly to the conventional lowpass-Favre filter for variable density flows, denoted as $\widehat{\phi} = \overline{\rho\phi}/\overline{\rho}$ with the over-bar $\overline{(\cdot)}$ representing the lowpass filter, the wavelet-Favre filter is defined as $\widehat{\phi}^{>\epsilon} = \overline{\rho\phi}^{>\epsilon}/\overline{\rho}^{>\epsilon}$, where the wavelet threshold filtering operator $\overline{(\cdot)}^{>\epsilon}$ is given by Eq. (18). In the wavelet-Favre filtered Navier-Stokes equations, consequently, the primitive variables are $\overline{\rho}^{>\epsilon}$, $\overline{p}^{>\epsilon}$, $\widehat{u_i}^{>\epsilon}$, $\widehat{T}^{>\epsilon}$, and $\widehat{e}^{>\epsilon}$, representing, respectively, the wavelet filtered density of the fluid (gas) and pressure, the wavelet-Favre filtered velocity, temperature and total energy per unit mass. For the sake of simplicity, the variables ρ, p, u_i, T, and e are used hereafter to denote all the primitive variables. Subsequently, the wavelet-Favre filtered Navier-Stokes equations for conservation of mass, momentum, and energy in compressible flows of calorically perfect gas with modeled turbulent terms can be written in the following form:

$$\frac{\partial \rho}{\partial t} + \frac{\partial (\rho u_j)}{\partial x_j} = 0, \tag{1}$$

$$\frac{\partial \rho u_i}{\partial t} + \frac{\partial}{\partial x_j}(\rho u_i u_j) = -\frac{\partial p}{\partial x_i} + \frac{\partial \hat{\tau}_{ij}}{\partial x_j}, \tag{2}$$

$$\frac{\partial \rho e}{\partial t} + \frac{\partial}{\partial x_j}[(\rho e + p)u_j] = \frac{\partial}{\partial x_j}[u_i \hat{\tau}_{ij} - q_j], \tag{3}$$

where

$$p = \rho R T, \tag{4}$$

$$e = \frac{1}{2} u_i u_i + \frac{p}{\rho(\gamma - 1)}, \tag{5}$$

$$q_j = -c_p \left(\frac{\mu}{Pr} + \frac{\mu_{\mathrm{T}}}{\mathrm{Pr}_{\mathrm{T}}} \right) \frac{\partial T}{\partial x_j}, \tag{6}$$

$$\hat{\tau}_{ij} = 2\mu \tilde{S}_{ij} - \tau_{ij}, \tag{7}$$

$$-\tau_{ij} = \rho \left(\widehat{u_i^{\mathrm{nf}} u_j^{\mathrm{nf}}}^{>\epsilon} - u_i u_j \right) = 2\mu_{\mathrm{T}} \tilde{S}_{ij},$$

$$\tilde{S}_{ij} = \mathrm{dev}(S_{ij}) = S_{ij} - \frac{1}{3} \frac{\partial u_k}{\partial x_k} \delta_{ij},$$

$$S_{ij} = \frac{1}{2} \left(\frac{\partial u_i}{\partial x_j} + \frac{\partial u_j}{\partial x_i} \right). \tag{8}$$

The parameter R is the gas constant, while c_v and c_p are the specific heat constants at constant volume and pressure, respectively. The specific heat ratio $\gamma = c_p/c_v \equiv 1.4$ for diatomic gases, and $\mathrm{Pr} = \mu c_p/\lambda$ is the Prandtl number, where λ is the thermal conductivity. The term q_j is the sum of both the laminar and modeled turbulent heat fluxes with $\mathrm{Pr} = 0.72$ and $\mathrm{Pr_T} = 0.9$ being the laminar and turbulent Prandtl numbers, respectively. The turbulent eddy viscosity is denoted by μ_{T}, which is unknown and needs a turbulence model for closure. The term $\hat{\tau}_{ij}$ is the sum of the molecular and SGS stress tensors, while S_{ij} is the mean strain-rate tensor, $\tilde{S}_{ij}$ is the deviatoric tensor of S_{ij}, δ_{ij} is the Kronecker δ, $-\tau_{ij}$ is the SGS stress tensor, and the summation convention for repeated indices is assumed. Note that the unclosed term $\widehat{u_i^{\mathrm{nf}} u_j^{\mathrm{nf}}}^{>\epsilon}$ is defined by the unfiltered velocity u_i^{nf}. The temperature-dependent dynamic molecular viscosity μ is given by the Sutherland's law,

$$\frac{\mu}{\mu_{\mathrm{ref}}} = \frac{T_{\mathrm{ref}} + S}{T + S} \left(\frac{T}{T_{\mathrm{ref}}} \right)^{3/2}, \tag{9}$$

where the constants $S = 110.4K$ and T_{ref} is the user-defined reference temperature.

B. The Anisotropic minimum dissipation SGS model

In this paper the anisotropic minimum dissipation (AMD) model proposed by Rozema *et al.* [30] is chosen as the SGS model for the WA-WMLES computations. The AMD eddy viscosity provides the minimum required dissipation to remove the SGS effects from the LES realizations and is given by

$$\mu_{\mathrm{T}} = \rho C_{\mathrm{AMD}} \frac{\max\left\{ -\left[\Delta_k \frac{\partial u_i}{\partial x_k} \Delta_l \frac{\partial u_j}{\partial x_l} \left(\frac{\partial u_j}{\partial x_i} + \frac{1}{2} \frac{\partial u_p}{\partial x_p} \delta_{ij} \right) \right], 0 \right\}}{\frac{\partial u_m}{\partial x_n} \frac{\partial u_m}{\partial x_n}}, \tag{10}$$

where $\Delta_k, k = 1, 2, 3$ denotes the mesh spacing in the $x_k, k = 1, 2, 3$, directions. Note an additional dilatation term $\frac{\partial u_p}{\partial x_p}$ in the numerator, which is absent in the original formulation of Rozema *et al.* [30]. This term is added for compressible flows to account for the density variation and the violation of divergence-free assumption on the velocity perturbation of the original derivation of Verstappen [31]. Also note, that in Eq. (10) the effect of turbulent kinetic energy transfer due to density stratification is neglected, i.e., in the derivation of Eq. (10) it is assumed that $|\mathbf{u}\nabla\rho| \ll \rho\|\nabla\mathbf{u}\|$.

The model coefficient is $C_{\mathrm{AMD}} = 0.212$ in most of the domain where the fourth-order central difference scheme is used while it is tuned to $C_{\mathrm{AMD}} = 0.3$ for the first two wall-normal points away

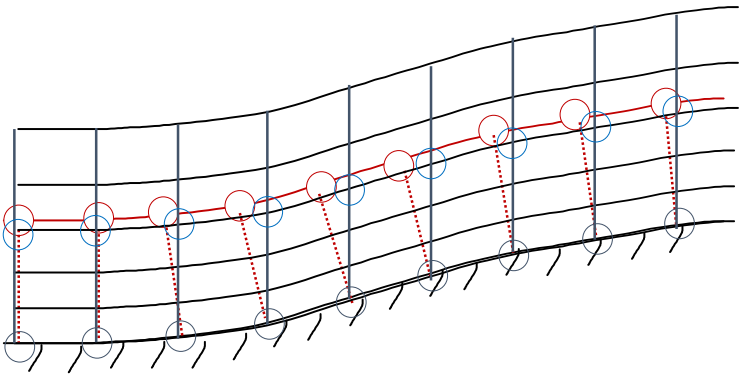

FIG. 1. An illustration depicting the nonorthogonal LES mesh, the closest LES mesh points (blue) to the exchange locations, and the boundary points for the RANS ODEs on the wall (black) and the exchange layer (red).

from the boundary where the second-order one-sided or central difference schemes are used. The justification of use of the lower-order schemes are discussed in Sec. III.

C. The inner-layer wall model

The separate inner-layer wall model used in this paper follows the work reported in Ref. [15,28], i.e., the equilibrium model. The model equations form a coupled system of ODEs, which read

$$\frac{d}{d\eta}\left[\left(\mu+\mu_{\mathrm{T}}^{\mathrm{wm}}\right)\frac{du^{||}}{d\eta}\right]=0,\ \frac{d}{d\eta}\left[\left(\mu+\mu_{\mathrm{T}}^{\mathrm{wm}}\right)u^{||}\frac{du^{||}}{d\eta}+\left(\frac{\mu}{\mathrm{Pr_L}}+\frac{\mu_{\mathrm{T}}^{\mathrm{wm}}}{\mathrm{Pr_T^{wm}}}\right)\frac{dT}{d\eta}\right]=0, \tag{11}$$

where η is the wall-normal coordinate, $u^{||}$ the wall-parallel velocity component and T is the temperature. This system of ODEs with specified boundary conditions is solved sequentially between $\eta=0$ and $\eta=\eta^{\mathrm{EL}}$ (η^{EL} is the wall-normal distance of the LES exchange location) using the Newton iteration method with the second-order central difference discretization, which forms a tridiagonal system. The boundary conditions at the wall at $\eta=0$ for the velocity and temperature are no-slip and isothermal and adiabatic and at exchange location at $\eta=\eta^{\mathrm{EL}}$ are $u^{||}=u^{||,\mathrm{EL}}$ and $T=T^{\mathrm{EL}}$. All boundary values at the exchange location are obtained following an interpolation procedure [28] from the closest LES mesh point to the exchange location using linear interpolation

$$u_i^{\mathrm{EL}}=u_i^{\mathrm{LES}}+\left.\frac{\partial u_i}{\partial x_j}\right|_{\mathrm{LES}}\left(x_j^{\mathrm{EL}}-x_j^{\mathrm{LES}}\right). \tag{12}$$

The use of interpolation Eq. (12) provides the flexibility to the LES mesh, which does not need to be orthogonal at the wall. An illustration is given in Fig. 1 depicting the nonorthogonal LES mesh, the closest LES mesh points to the exchange locations, and the boundary points for the RANS ODEs on the wall and the exchange layer.

The wall-model eddy viscosity $\mu_{\mathrm{T}}^{\mathrm{wm}}$ follows the mixing-length model adopted in Ref. [15] and is given by

$$\mu_{\mathrm{T}}^{\mathrm{wm}}=\kappa\eta\sqrt{\rho\tau_w}\left[1-\exp\left(-\frac{\eta^+}{A^+}\right)\right], \tag{13}$$

where $A^+=17$ and $\kappa=0.41$. The turbulent Prandtl number is $\mathrm{Pr_T^{wm}}=0.9$.

D. The LES boundary conditions

The shear stress at the wall is assumed to be aligned with the wall-parallel velocity at the EL, i.e., making the assumption that the shear stress direction remains unchanged across the unresolved part of the boundary layer, which gives

$$(\hat{\tau}_{ij} n_j)_w^{\mathrm{LES}} = \tau_w^{\mathrm{wm}} e_i^{||}, \tag{14}$$

where $e_i^{||}$ is the unit vector parallel to the wall and aligned with $u_i^{||,\mathrm{EL}}$, n_j is the unit vector normal to the wall and τ_w^{wm} is the wall shear stress value returned from the equilibrium wall model. Similarly, the heat flux at the wall is given by

$$(q_j n_j)_w^{\mathrm{LES}} = q_w^{\mathrm{wm}}, \tag{15}$$

with q_w^{wm} being the heat flux scalar returned from the equilibrium wall model. Note that the total stress and heat flux terms $\hat{\tau}_{ij}$ and q_j, defined by Eqs. (7) and (6), are used in these boundary condition formulations. Due to the equilibrium assumption of the wall model the wall pressure is assumed to be the same as the pressure at the exchange location, i.e., p^{EL}, or equivalently

$$\left(\frac{\partial p}{\partial x_j} n_j\right)_w^{\mathrm{LES}} = 0, \tag{16}$$

which can be rewritten as Robin-type boundary condition for the density. Thus, the WA-LES Eqs. (1), (2), and (3) are solved with density, velocity, temperature, and viscous and heat fluxes at the wall calculated from the no-penetration $u_j n_j = 0$, shear stress Eq. (14), heat flux Eq. (15) boundary conditions, and the equilibrium assumption for the wall pressure.

III. NUMERICAL METHODS

A. Wavelet-based adaptive computations

The wavelet-based adaptive wall-modeled LES method described above is implemented using the parallel adaptive wavelet-based collocation method (PAWCM) [8]. The PAWCM is based on multiresolution wavelet analysis to construct time-dependent computational meshes with spatially varying resolution that is required to adequately resolve the localized structures of the solution with *a priori* prescribed accuracy. From previous studies on different wavelet-based turbulence modeling methods for linearly forced homogeneous turbulence [32] and supersonic channel flow [24] the Reynolds number scaling of wavelet-based adaptive methods is considerably slower than cubic, i.e., Re^3, required for the nonadaptive DNS. The study of the Re scaling of the WA-LES and WA-MWLES at high Reynolds numbers is the subject of future investigation, since the primary objective of the current work is to expand the application of the wavelet-based algorithms to simulation of high Reynolds number flows.

The mesh adaptation in PAWCM is based on the analysis of wavelet decomposition of a spatially dependent field, say $u(\mathbf{x})$, sampled on a set of dyadic nested collocation points $\mathbf{x}_{\mathbf{k}}^j$ at different levels of resolution j, formally written as

$$u(\mathbf{x}) = \sum_{\mathbf{l}\in\mathcal{L}^1} c_{\mathbf{l}}^1 \phi_{\mathbf{l}}^1(\mathbf{x}) + \sum_{j=2}^{J} \sum_{\mu=1}^{2^n-1} \sum_{\mathbf{k}\in\mathcal{K}^{\mu,j}} d_{\mathbf{k}}^{\mu,j} \psi_{\mathbf{k}}^{\mu,j}(\mathbf{x}), \tag{17}$$

where n denotes the number of spatial dimensions, bold subscripts denote n-dimensional indices, while $\mathcal{L}^1$ and $\mathcal{K}^{\mu,j}$ are n-dimensional index sets associated with scaling functions $\phi_{\mathbf{l}}^1$ and different family wavelets $\psi_{\mathbf{k}}^{\mu,j}$, respectively. Each of the basis functions, i.e., $\phi_{\mathbf{l}}^1$ or $\psi_{\mathbf{k}}^{\mu,j}$, has one-to-one correspondence with a mesh point $\mathbf{l} \in \mathcal{L}^1$ or $\mathbf{k} \in \mathcal{K}^{\mu,j}$. Scaling functions $\phi_{\mathbf{l}}^1$ carry the averaged signal, while the multidimensional second-generation wavelet functions $\psi_{\mathbf{k}}^{\mu,j}$ define local, variational details. The amplitudes are given by the coefficients $c_{\mathbf{l}}^1$ and $d_{\mathbf{k}}^{\mu,j}$, respectively, and hence have a

unique correspondence to mesh points. The levels of resolution span over $1 \leqslant j \leqslant J$, with 1 and J being, respectively, the coarsest and finest levels of resolution present in the approximation. During the wavelet transform, detail (or wavelet) coefficients $d_{\mathbf{k}}^{\mu,j}$ are obtained recursively from scaling function coefficients $c_{\mathbf{k}}^{\mu,j}$ from level J to 2. After the wavelet transform, the coefficients $c_{\mathbf{l}}^{1}$ ($\mathbf{l} \in \mathcal{L}^1$) and $d_{\mathbf{k}}^{\mu,j}$ ($\mathbf{k} \in \mathcal{K}^{\mu,j}$) are stored, respectively, at the mesh points of the coarsest ($j = 1$) and higher ($2 \leqslant j \leqslant J$) levels of resolution. Note that for n-dimensional space, there are $2^n - 1$ families of wavelet functions, indexed by μ.

Wavelet threshold filtering arises naturally from the series expansion (17). The filtering operation is performed by applying the wavelet transform to the original field $u(\mathbf{x})$, zeroing the wavelet coefficients below a given threshold, $\epsilon = \epsilon(\mathbf{x}, t)$ for generality, and transforming back to the physical space. The resulting approximate field, say $u^{>\epsilon}(\mathbf{x})$, composed of a subset of the original wavelets, represents the dominant modes and can be formally written as the following conditional series:

$$u^{>\epsilon}(\mathbf{x}) = \sum_{\mathbf{l}\in\mathcal{L}^1} c_{\mathbf{l}}^{1}\phi_{\mathbf{l}}^{1}(\mathbf{x}) + \sum_{j=2}^{J}\sum_{\mu=1}^{2^n-1}\sum_{\substack{\mathbf{k}\in\mathcal{K}^{\mu,j} \\ |d_{\mathbf{k}}^{\mu,j}|>\epsilon\|u(\mathbf{x})\|}} d_{\mathbf{k}}^{\mu,j}\psi_{\mathbf{k}}^{\mu,j}(\mathbf{x}). \tag{18}$$

In many implementations, the filter threshold is taken to be relative to some characteristic scale, often represented by either the L_2 or L_∞ norm of $u(\mathbf{x})$ taken globally over the domain and denoted as $\|u(\mathbf{x})\|$ [3]. The resulting nonlinear filtering operation practically separates resolved flow structures and unresolved residual motions. For a properly normalized threshold, the reconstruction error of the filtered variable is shown [33] to converge as

$$\|u^{>\epsilon} - u\| \leqslant C\epsilon\|u\|, \tag{19}$$

where $C = O(1)$.

The dynamic mesh adaptation is tightly coupled with the wavelet filter. Due to the one-to-one correspondence between wavelets and grid points, the nodes are omitted from the computational mesh if the associated wavelets are excluded from the truncated approximation Eq. (18). The multilevel structure of this wavelet approximation provides a natural way to obtain the solution on a nearly optimal numerical mesh, which is dynamically adapted to the evolution of the main flow structures, both in location and scale, while higher resolution computations are carried out in the regions where (and only where) steep gradients in the resolved flow field occur.

The multiresolution wavelet decomposition Eq. (18) is used for both mesh adaptation and interpolation, while a hierarchical finite difference scheme [9,10], which takes advantage of the wavelet interpolating properties, is used to numerically differentiate the local function approximations and to provide the values of derivatives at the adaptive computational nodes.

Second-generation wavelet bases, described above, rely on topologically rectilinear mesh and inherently isotropic mesh elements. This restriction puts some limitations on the applicability of the approach for simulation of complex geometry wall-bounded turbulent flows. These limitations were recently overcome with the development of the A-AWCM [7]. The A-AWCM preserves active error-controlling properties of the original AWCM [8–11], but provides an additional flexibility to control mesh anisotropy and to solve the problem in complex domains by separating the computational space from the physical one and introducing a mapping between them, thus, allowing the use of anisotropic curvilinear meshes in complex geometries. At the same time, the structured rectilinear assembly of collocation points in the computational space is retained, which allows the use of computationally efficient discrete adaptive wavelet transform and derivative approximations.

B. Numerical implementations for the WA-WMLES

1. Wall model implementation

The numerical implementation for the inner layer modeling computations in the WA-WMLES method consists of the following steps:

(i) Impose viscous and heat flux boundary conditions Eqs. (14) and (15) using wavelet-based finite difference scheme on curvilinear mesh, resulting in a linear algebraic system of equations that relates the velocity u_i and temperature T at the wall and neighboring internal points. These modified wall velocity and temperature are unphysical and, hence, are not appropriate for evaluation of the convective fluxes for the density, momentum, and energy as well as the viscous power term $u_i\hat{\tau}_{ij}$ in the energy equation. As suggested by Kawai and Larsson [15], these flux terms are set to zero at the wall. In addition, the molecular viscosity at wall points is directly obtained from the equilibrium wall-model computation rather than evaluated from the modified wall temperature values using Eq. (9).

(ii) Update the wall shear stress τ_w^{wm} and heat flux q_w^{wm} returned from the equilibrium wall model before each LES time integration. To minimize the computational cost the no-penetration and wall flux boundary conditions are imposed on the solution fields only for the first stage of the three-stage Runge-Kutta (RK3-TVD) time integration scheme without performing the equilibrium wall-model computations for intermediate stages of the time integration. As pointed out in Ref. [28] the effect of this simplification on the accuracy is negligible. For the remaining RK stages, conserved variables, i.e., density, momentum and internal energy on the wall are updated directly using the RK3-TVD time integration scheme for the intermediate-stage solution fields. For the other regular boundaries, such as inflow and outflow as well as inviscid or free-stream boundaries, the corresponding boundary conditions are applied for all-three-stage solutions.

(iii) Use second-order one-sided and central difference schemes on the first and second points away from the wall, respectively, when calculating the viscous flux terms. The wall values of u_i and T obtained in step (i) are only used to impose the desired viscous fluxes at the wall and not accurate for calculating the gradients invoked in the viscous fluxes for the wall-adjacent points. Therefore, as suggested by Kawai and Larsson [15], the second-order one-sided and central difference schemes are used on the first and second points away from the wall, respectively. At other points, the standard wavelet-based hierarchical fourth-order central difference scheme is used. Although the second-order schemes reduce the accuracy of viscous flux calculation at the first and second points away from the wall, the solution at these points is always highly under-resolved due to the coarse mesh in the wall-normal direction no matter how accurate the numerical scheme is. The key point for WMLES is that the wall viscous fluxes are intended to be accurate away from the wall and the LES solution at the exchange layer is well resolved and uses high-order numerical scheme.

(iv) Impose the no-penetration boundary condition for the wall velocity after the final stage of the RK3-TVD for each time step.

(v) Map the points within the LES domain closest to the exchange-location (EL) points to the wall points.

(vi) Distribute the equilibrium wall-model calculations evenly among all the parallel processes to guarantee load-balancing for the equilibrium wall-model computations. The CPU time of the equilibrium wall-model computation including the MPI communication is around 10% of the total CPU time required for each time step integration.

(vii) Synchronize the results of equilibrium wall-model calculations between all the parallel processes. After the wall stress and heat flux are returned from the equilibrium wall-model solver, these data are redistributed to corresponding processors that contain wall points for the LES computation.

(viii) Enforce the nonadaptive under-resolved mesh near the wall below the exchange location to reduce the total degrees of freedom effectively and to turn-off mesh adaptation in the inner layer region.

TABLE I. Strong scalability test for the three-dimensional WA-WMLES simulations of flat plate turbulent boundary layer with approximately 10 million adaptive mesh points. Data are based on CPU time for fixed time steps.

No. cores	No. points/core	Speed up	Efficiency
28	371 K	28	1
56	186 K	56	1.00
112	93 K	101	0.90
224	46 K	187	0.84
448	23 K	251	0.56

2. Parallel algorithm

The parallel algorithm for the A-AWCM [8] is also briefly introduced in this section. The domain is partitioned using the Zoltan partitioning library [34] from Sandia National Laboratories. Zoltan geometric (recursive coordinate bisection) and Zoltan hypergraph parallel partitioning algorithms are used. Dynamic load balancing is implemented via domain repartitioning during the grid adaptation step and reassigning tree data structure nodes to the appropriate processes. The user provides an imbalance tolerance vector to trigger the repartitioning if necessary. The type of repartitioning depends on the imbalance of the wavelet distribution. Highly imbalanced data are partitioned without considering current decomposition, moderately imbalanced data are repartitioned while trying to stay close to the current decomposition, and nearly balanced data are refined by small changes only. For detailed discussions about the parallelization the reader is referred to Ref. [8].

To demonstrat the scalability of the parallel A-AWCM implementation, a 3D WA-WMLES of a flat pate turbulent boundary layer (TBL) flow with inflow $\mathrm{Re}_\theta = 7000$ and Mach number $\mathrm{Ma} = 0.3$ is tested. The simulations with approximately 10 million adaptive mesh points have been performed on the Bridges system at Pittsburgh Supercomputing Center, part of the Extreme Science and Engineering Discovery Environment (XSEDE). Details of the mesh setup are given in Sec. IV A. The corresponding strong scaling data are shown in Table I. The deterioration of the performance is observed when the number of grid points per core drops below 2×10^4, which is also consistent with the results reported in Ref. [8] for linearly forced homogeneous turbulence.

IV. SIMULATIONS AND RESULTS

A. Zero pressure gradient flat plate turbulent boundary layer flow

1. Numerical setup

To demonstrate the effectiveness and accuracy of the WA-WMLES method we start by considering a subsonic zero pressure gradient flat plate turbulent boundary layer flow, which also used for validation of inflow conditions, required for more complex flow presented later. The computational domain size is $28\delta \times 14\delta \times 4.8\delta$ in streamwise, wall-normal, and spanwise directions, respectively, where δ is the boundary layer thickness at the inflow plane. The effective mesh resolution for the WA-WMLES is $2560 \times 192 \times 512$ with seven levels of resolution, base (coarsest level) resolution of $40 \times 3 \times 8$, uniform mesh spacing in the wall-tangential directions, and stretched mesh with a hyperbolic tangent distribution in the wall-normal direction. The wall-parallel mesh spacings at the finest level are $\Delta x^+ \approx 23$ and $\Delta z^+ \approx 20$. The smallest allowed wall-normal mesh spacing is about $\Delta y^+ \approx 17$. Note that, in the actual implementation, the initial adaptive mesh is either generated starting from a uniform coarse mesh at a user-defined lowest allowed level of resolution $j_{\min}$ (usually 2) and is recursively refined wherever it is necessary up to the finest allowed level based on the user-defined initial condition or imported from existing wavelet-based adaptive simulations so that the initial mesh is usually even coarser than the final adaptive mesh when the flow is fully developed. In other words, the initial mesh is already adaptive and does not use unnecessary mesh points.

A locally nonadaptive under-resolved mesh region at level $j = 6$ is specified between the wall and the wall-parallel plane at $y/\delta = 0.035$ with the height of the EL points being 0.092δ (about $y^+ = 180$ at the inlet). To test the sensitivity of the results to the EL height the value of 0.035δ (about $y^+ = 60$ at the inlet) is also tested, but a significant log-layer mismatch is observed (not shown). As explained by Kawai and Larsson [15] this is mostly due to feeding into the equilibrium wall model the under-resolved LES solution with only two mesh points present between the wall and the EL location at level $j = 6$.

Freund's sponge zone [35] is imposed for the nonreflective conditions at the top and outflow boundaries, with zone thicknesses of 1.0δ and 2.0δ, respectively. For the Freund's zone parameters, to accelerate the convection of the flow structures out of domain the artificial convective velocity is chosen to be at supersonic speed $1.2a_\infty$, where a_∞ is the free-stream speed of sound. The damping term coefficient is set to be $2a_\infty/D$, where D is the characteristic length of the domain. The higher this parameter, the more backflow structures are dissipated out before entering the physical domain. The target fields for the sponge zones at these two boundaries are the ensemble-averaged fields of the resolved solutions. The periodic condition is imposed in the spanwise direction.

At the inflow, the local one-dimensional inviscid (LODI) relations [36] of the Navier-Stokes characteristic boundary conditions (NSCBC) are used for derivation of a linearised Navier-Stokes equation for the evolution of the density fluctuation with the characteristic out-going velocity and other linear coefficients being evaluated by the ensemble-averaged solution. This provides a soft boundary condition for the density. Note that in the actual implementation, the ensemble-averaged solution uses the initial condition (a RANS solution as described later) during the early stage of the simulation and then it switches to the calculated running time-average solution, once the time-average fields sufficiently converge. The velocity inflow conditions are the mean profiles plus the fluctuation components obtained from a synthetic turbulence generator (STG) [37]. The mean velocity profiles at the inflow are obtained from an incompressible LES solutions [38] at $\mathrm{Re}_\theta = 7000$. A low free-stream Mach number $\mathrm{Ma} = 0.3$ is assumed for this case and therefore a uniform temperature with an error of about 1.5% is imposed at the inflow plane. The inconsistency of the incoming pressure perturbations with zero temperature fluctuation and outgoing acoustic waves with nonzero temperature fluctuations is absorbed in the characteristic-based density fluctuations at the inflow. For moderate and high Mach number simulations, this method should be improved by introducing the temperature fluctuations using the Morkovin's strong Reynolds analogy [39].

STG inflow conditions consist of a superposition of spatiotemporal Fourier modes with random amplitudes and phases. It should be noted that the lateral size of the energy containing structures, created by the STG at the inflow, is small in the inner layer and large in the outer layer. In addition, the time-dependent synthetic velocity fluctuations, imposed at the inflow plane are convected with a global (bulk) velocity, which results in roughly the same streamwise size for all the vortical structures downstream of the inflow. The combination of these two features determines the formation of strongly anisotropic (elongated) eddies near the wall and nearly isotropic eddies away from the wall. Note that the invoked global (uniform) velocity is a macroscale velocity parameter in the formulation of this STG approach [37] to artificially construct desired flow structures and is intentionally chosen to be considerably larger than the streamwise convective velocity, which varies in the wall-normal direction. One significant advantage of STG approach [37] is that the transition length, required for the incoming turbulent boundary layer to become fully developed, is about 2 to 4 boundary layer thicknesses compared to 5 to 20 boundary layer thicknesses required in the digital filter-based (DFB) approach adopted in Ref. [40].

A nonlinear CFL-type restriction based on the sum of the local flow velocity and speed of sound is used to control the integration time step for the RK3-TVD scheme.

With exception of the nonadaptive under-resolved mesh region near the wall, the mesh adaptation in the rest of the domain is based on magnitude of wavelet coefficients of control variables satisfying criteria $|d_{\mathbf{k}}^{\mu,j}| > \epsilon \|u(\mathbf{x})\|$ as in Eq. (18) with a relative wavelet filtering threshold ϵ and the L_2 norms of the corresponding variables used as an absolute threshold. A zonal distribution of the wavelet

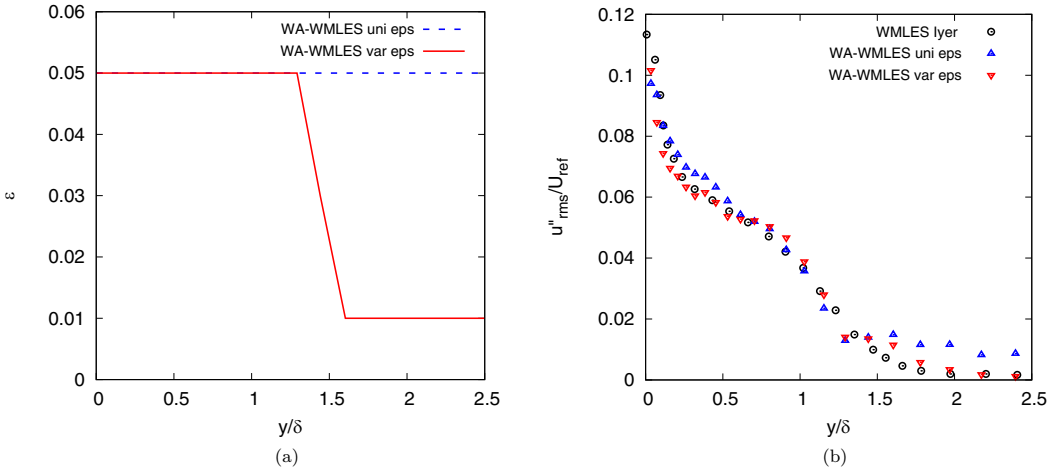

FIG. 2. Wall-normal profiles at a streamwise location $x/\delta = 24$ downstream of the inlet of the flat boundary layer case with uniform and zonal variable ϵ for the WA-WMLES method. (a) Wavelet threshold ϵ for momentum and total energy. (b) Time and spanwise averaged u''_{rms}. Comparison is made with the data reported by Ref. [40].

threshold ϵ field used for adaptation on momentum and total energy fields with distinct values of $\epsilon = 0.01$ and $\epsilon = 0.05$ in the inviscid and viscous zones is shown in Fig. 2(a). These two specific values of ϵ are conservatively chosen based on previous work [2,6,41], where a systematic grid convergence and parameter study for ϵ was conducted for the WA-LES approach. For the wall-bounded turbulent flows the wavelet threshold parameter in the range $\epsilon \in [0.01, 0.1]$ with the similar grid spacing in the wall-parallel directions was recommended.

The variation of pressure is much smaller than that of the momentum and total energy in the low Mach number flow, and hence to resolve the pressure more accurately smaller values of $\epsilon = 0.005$ and $\epsilon = 0.001$ are used in the viscous and inviscid zone, respectively. A relatively small value of the ϵ outside of the boundary layer is used to remove unphysical perturbations associated with the ϵ-bounded relative error in the inviscid region. These perturbations are present if a uniform wavelet threshold is used. This is illustrated in Fig. 2(b), where the streamwise velocity root mean square $u''_{\text{rms}} \gtrapprox 0.01U_{\text{ref}}$ outside of the boundary layer is observed when a uniform $\epsilon = 0.05$ for momentum is used throughout the domain as opposed to approaching zero when smaller value of ϵ is used outside the boundary layer region. Moreover, this zonal treatment of ϵ also improves the result in the boundary layer region, which is depicted in Fig. 3(a) showing the difference between two WA-WMLES computations with uniform $\epsilon = 0.05$ (the blue line) and zonal distribution of ϵ (the red line). Better correspondence of the WA-WMLES results using the zonal wavelet threshold with the reference WA-URANS results is observed. Finally, it should be pointed out that in addition to adapting on flow variables the mesh is also adapted on the physical coordinates with uniform $\epsilon = 0.005$.

2. Simulation results

The resulting adaptive mesh contains about 7.0 million points for the zonal ϵ with the corresponding compression ratio of 97.2%, defined as the percentage of discarded wavelets with respect to the nonadaptive case. It is interesting to note that the adaptive mesh with uniform ϵ uses about 6.5 million nodes, which is just slightly coarser than the former, thus, justifying the efficiency of using smaller ϵ in the inviscid region where solution is relatively smooth. The zonal treatment of ϵ for the newly developed WA-WMLES method is consistent with previously published studies on WA-WRLES with variable thresholding [5] and WA-DDES [24,25], where different values of

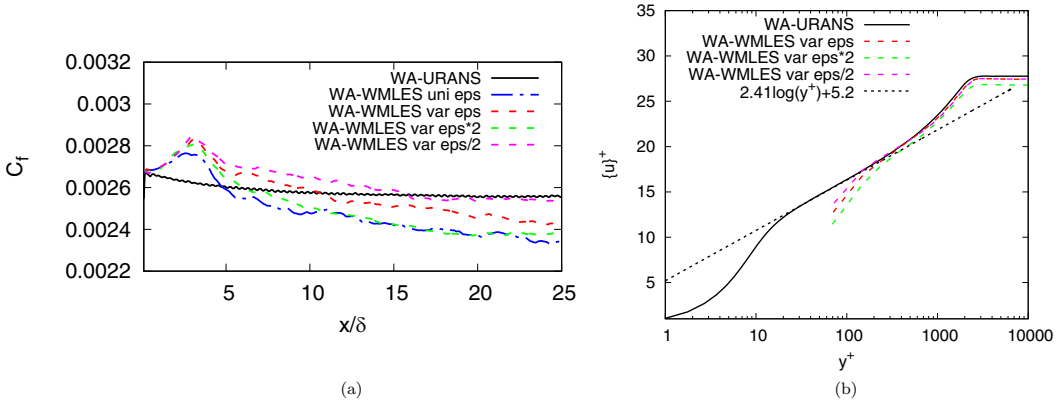

FIG. 3. Result comparison of the flat plate turbulent boundary layer case with uniform and different zonal variable ϵ for the WA-WMLES method. (a) Time and spanwise averaged skin friction distributions. (b) Time and spanwise averaged streamwise velocity profiles in the inner-layer scale.

wavelet threshold were used in WA-URANS and WA-LES regions. A similar issue in identifying the height of the exchange-layer exists for all prevailing WMLES methods, where an *a priori* defined boundary layer thickness is used to determine the the EL height. Further investigation on the use of variable threshold ϵ that depends on the solution, e.g., the vorticity field, and identifies the inviscid and viscous flow regions is deferred for a future work.

Note that due to adaptive nature of the PAWCM, marginally resolved simulations as the non-adaptive WMLES case result in aliasing errors that spread and considerably increase the number of adaptive mesh points used in the simulations, as opposed to the well-resolved calculations with very fine mesh at the effectively highest resolution. Therefore, for the grid convergence study, the nonadaptive WMLES requires adjustment of grid spacings while the WA-WMLES usually uses different values of wavelet threshold since the grid spacings at the effectively highest resolution are already very small and even at the level comparable to some nonadaptive WRLES. Meanwhile, the adaptation induced error between the wavelet-based adaptive mesh and the full mesh at the highest resolution is controlled by the wavelet threshold [cf. Eq. (19)]. To demonstrate the grid convergence of WA-WMLES, the simulations for the flow configuration shown in Fig. 2(a), but with doubled and halved wavelet thresholds ϵ are conducted. A summary of different wavelet thresholds with corresponding numbers of adaptive mesh points to demonstrate the sensitivity of the results on ϵ in the viscous zone is given in Table II. The wavelet threshold in the inviscid zone is kept unchanged.

Figure 3(a) plots the mean skin friction distributions over the wall predicted by different wavelet threshold ϵ. The time averaged statistics are accumulated within a period of about $25\delta/U_{\text{ref}}$. The spanwise averaged statistics are computed by interpolating the continuous wavelet basis onto 2D, nonadaptive sampling mesh at level $j = 5$, and averaging across multiple slices in the streamwise and wall-normal plane. As mentioned above, the uniform ϵ case produces relatively poor results

TABLE II. Wavelet thresholds ϵ used in different variables for the hump flow.

Threshold ϵ	Momentum Inviscid/Viscous	Energy Inviscid/Viscous	Pressure Inviscid/Viscous	No. mesh points
Uniform	0.05/0.05	0.05/0.05	0.005/0.005	6.5 million
Baseline	0.01/0.05	0.01/0.05	0.001/0.005	7.0 million
Doubled	0.01/0.10	0.01/0.10	0.001/0.010	4.2 million
Halved	0.01/0.025	0.01/0.025	0.001/0.0025	18.2 million

due to the error related to the presence of acoustic waves in the inviscid zone, despite the use of the same value of ϵ in the viscous zone as the baseline case. The results for the doubled ϵ case are similar to the uniform ϵ case since high ϵ used in the viscous zone induces large errors, but, in turn, results in fewer adaptive mesh points. The halved ϵ case corresponds to the smallest error associated with the mesh adaptation and hence predicts the most accurate results compared to the reference WA-URANS simulation results at the expense of substantial increase of the adaptive mesh points (18.2 million), which, in general, is too large to be considered as an effective WMLES computation. However, since the error in the prediction of skin friction coefficient for the baseline zonal ϵ case is within 5%, it is sufficiently acceptable to compromise between the accuracy and the computational efficiency.

The comparison of mean streamwise velocity profiles in the inner-region at a station 10δ downstream of the inflow plane is given in Fig. 3(b). The following notations for averaged and fluctuating components are adopted in this paper: $\{\phi\} = \langle\rho\phi\rangle/\langle\rho\rangle$ and $\phi'' = \phi - \{\phi\}$ denote, respectively, Favre average and fluctuating quantities, while a Reynolds average quantity is denoted as $\langle\phi\rangle$. Good agreement between the WA-WMLES results and the reference WA-URANS data validates both the WA-WMLES approach and the STG inflow conditions. The results of the simulation demonstrate that computational domain with about 10 times the boundary layer thickness of the inflow plane is sufficient for turbulent boundary layer simulations with the STG inflow conditions, which is consistent with the prior STG studies [37,42] for the wall-resolved LES and DNS.

Moreover, the difference between results using different zonal ϵ is minimal, especially for the baseline and low ϵ cases. This also suggests that the use of the baseline ϵ is appropriate in terms of accuracy and efficiency.

The maximum CFL number is set to be 0.7 over the entire domain with the resulting time step $\Delta t \approx 1.0 \times 10^{-3}\delta/U_{\text{ref}}$, where U_{ref} is the free-stream reference velocity. This time step is around one to two orders of magnitude larger than that of the WA-DDES method [24] for a boundary layer flow at the same Reynolds number, which implies a significant reduction of total numbers of time integration steps and, hence, the overall computational cost. For the current WA-WMLES simulation, 224 cores as shown in Table I are used, which results in 10 s per time integration. It requires about $25\delta/U_{\text{ref}}$ time interval for statistical convergence. Therefore, it takes about 15.5×10^3 CPU core hours (224 cores $\times[10/3600 \times 25/(1 \times 10^{-3})]$ h).

The per point cost of adaptive simulations is three times more expensive for the PAWCM compared to the nonadaptive simulations, which makes the adaptive method in principle outperform the corresponding nonadaptive one when less than 33% of the mesh points are retained in the calculation. Therefore, once the compression ratio exceeds 67%, the computation on the adaptive mesh becomes cheaper than on the nonadaptive finest mesh. For the results reported in both previous [2,6,24,27,41] and current work the compression ratios above 90% are observed for most of three-dimensional cases. However, due to inherent overhead from the buffer zone communication among cores in the parallel algorithm proposed in Ref. [8] the MPI synchronization procedures during parallel wavelet transform and derivative calculations may be the bottle neck for efficiency of the PAWCM compared to other nonadaptive and simple data structure methods in practice. Further improvement of the PAWCM is under investigation and out of scope of this work.

The adaptive mesh colored by the levels of resolution is presented in Fig. 4. Figure 5 displays the Q-criterion isosurface colored by the instantaneous spanwise momentum. A zoom-in slice in the streamwise and wall-normal plane of the adaptive mesh with the streamwise momentum contours on the background is illustrated in Fig. 6. WA-WMLES results demonstrate that most of the adaptive mesh points in the lower part of the boundary layer are on level $j = 6$ with few scattered nodes on the finest level $J = 7$. In the upper region of the boundary layer due to significant increase in the length scale of the flow structures most of the adaptive grid points belong to levels $j = 4$ and 5.

The mean velocity profile and the turbulence statistics at a streamwise location $x/\delta = 24$ downstream of the inlet are plotted in Fig. 7. The WA-WMLES results are compared with nonadaptive WMLES results of Iyer and Malik for the flat plate turbulent boundary layer upstream of a wall-mounted hump with the same inflow Re_θ (case fWM3 in Ref. [40]). The agreements of these profiles

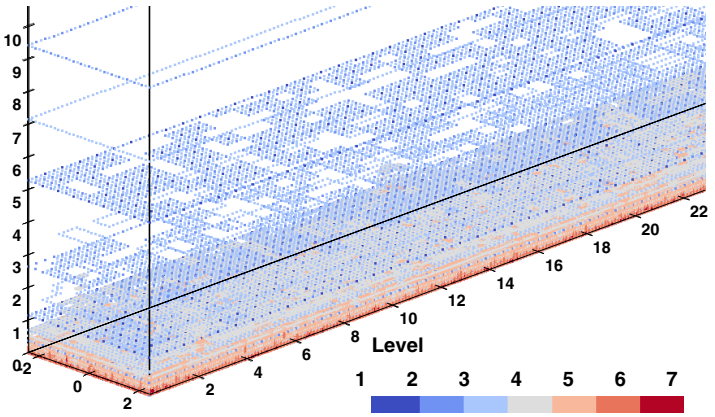

FIG. 4. The adaptive mesh colored with levels of resolution for the subsonic flat plate turbulent boundary layer flow. Axis labels are in the unit of the boundary layer thickness at the inflow.

between the WA-WMLES and the reference WMLES are fairly acceptable. The discrepancies may be attributed to the different free-stream Mach numbers (Ma = 0.3 versus Ma = 0.1 in Ref. [40]) and inflow turbulence generation techniques. In addition, there is an artificial hump or plateau in the profile of streamwise turbulent normal stress $\{u''u''\}$ around the edge of the boundary layer, as shown in Fig. 7(c). This attributes to the sudden switch of wavelet thresholds as demonstrated in Fig. 2(a) with the same issue also observed in Fig. 2(b).

B. Separated flow over NASA's wall-mounted hump

The second flow configuration used for demonstration of the WA-WMLES method involves a wall-mounted hump geometry, also known as the 2D NASA hump case, representative of the upper surface of an airfoil. It represents the NASA Revolutionary Computational Aerosciences (RCA) standard test case. The original experimental study of this problem is reported in Ref. [43]. The computational configuration in this work mainly follows the NASA 2004 CFD Validation Workshop [44] and represents the baseline validation case with no plenum for flow control. An adverse pressure

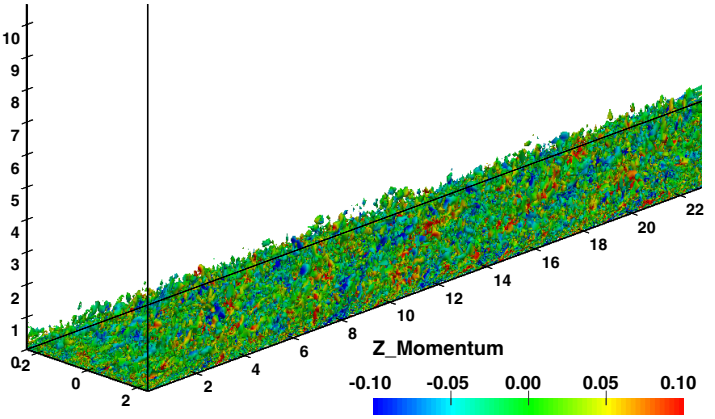

FIG. 5. The instantaneous Q-criterion isosurface colored by instantaneous spanwise momentum for the subsonic flat plate turbulent boundary layer flow. Axis labels are in the unit of the boundary layer thickness at the inflow.

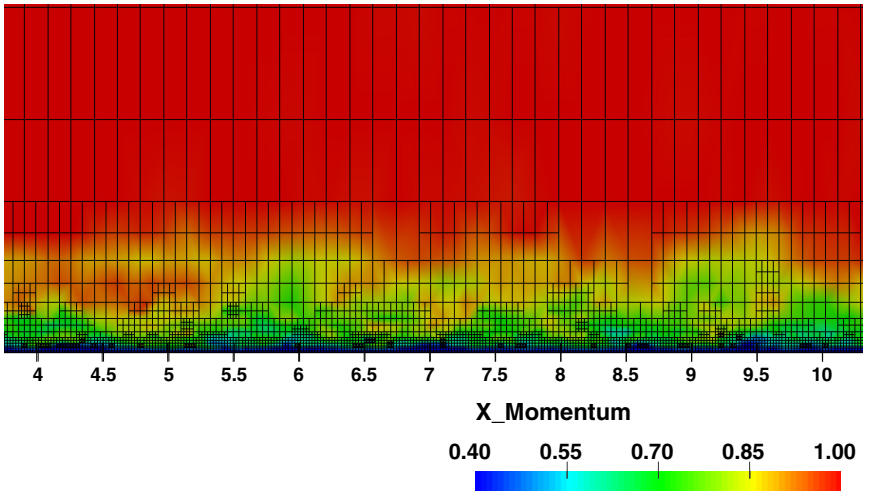

FIG. 6. Zoomed-in view of a slice in the streamwise and wall-normal plane of the adaptive mesh with the streamwise momentum contours for the subsonic flat plate turbulent boundary layer flow in the background. Axis labels are in the unit of the boundary layer thickness at the inflow.

gradient downstream of the hump causes the boundary layer separation. The experimental setup includes end plates attached to both sides of the wall hump model. Following most of numerical studies for this test case, the flow blockage effect of the end plates is mimicked by a specially contoured inviscid top wall. The top wall profile is suggested and provided by the NASA Turbulence Modeling Resource (TMR) [45] website in form of discretized coordinates. The low-speed flow upstream of the hump corresponds to a fully developed turbulent boundary layer flow with hump-chord (c)-based Reynolds number of $\mathrm{Re} = 936\,000$. To minimize computational resources caused by CFL time step limitation the incoming free stream Mach number of $\mathrm{Ma} = 0.2$ for WA-WMLES is used instead of $\mathrm{Ma} = 0.1$, observed in the experiment. The reference static pressure (p_{ref}) is located at $x/c = -2.14$, while the leading edge of the hump is defined at $x/c = 0$.

1. Numerical setup

The domain size and the boundary conditions are as follows. The streamwise domain spans from $x/c = -2.14$ to $x/c = 4$ with the contoured hump located between $x/c = 0$ and $x/c = 1$. Following the nonadaptive WMLES simulation in Ref. [40], the spanwise size is chosen to be $0.3c$.

A standard k-ω SST model-based steady RANS auxiliary computation is performed with the mesh size 817×217 posted on the TMR [46] website using the open source NASA code CFL3D. [47] This RANS solution is then utilized as the initial condition for the WA-WMLES computation. The CFL3D RANS results are first interpolated on to a 2D dyadic nested wavelet collocation mesh in the x-y plane, then extruded to the 3D domain along the spanwise direction. The time integration step is around $5.4 \times 10^{-5}\, c/U_{\mathrm{ref}}$ using the RK3-TVD scheme with the maximum CFL number set to 1.0.

The boundary conditions are similar to the flat plate turbulent boundary layer flow presented in Sec. IV A. Freund's sponge zone of thickness c is imposed for the nonreflective conditions at the outflow boundary. The target fields for the sponge zones at these two boundaries are the initial RANS fields. The periodic condition is imposed in the spanwise direction. At the inflow, the LODI NSCBC are used with the mean velocity and temperature profiles from the RANS solution. Note that the RANS solution extends its inflow plane upstream of the leading edge of the flat plate. The inflow profiles for the WA-WMLES computation are directly extracted at location $x/c = -2.14$. Due to different Mach numbers between the auxiliary RANS and the experiments, the slight difference

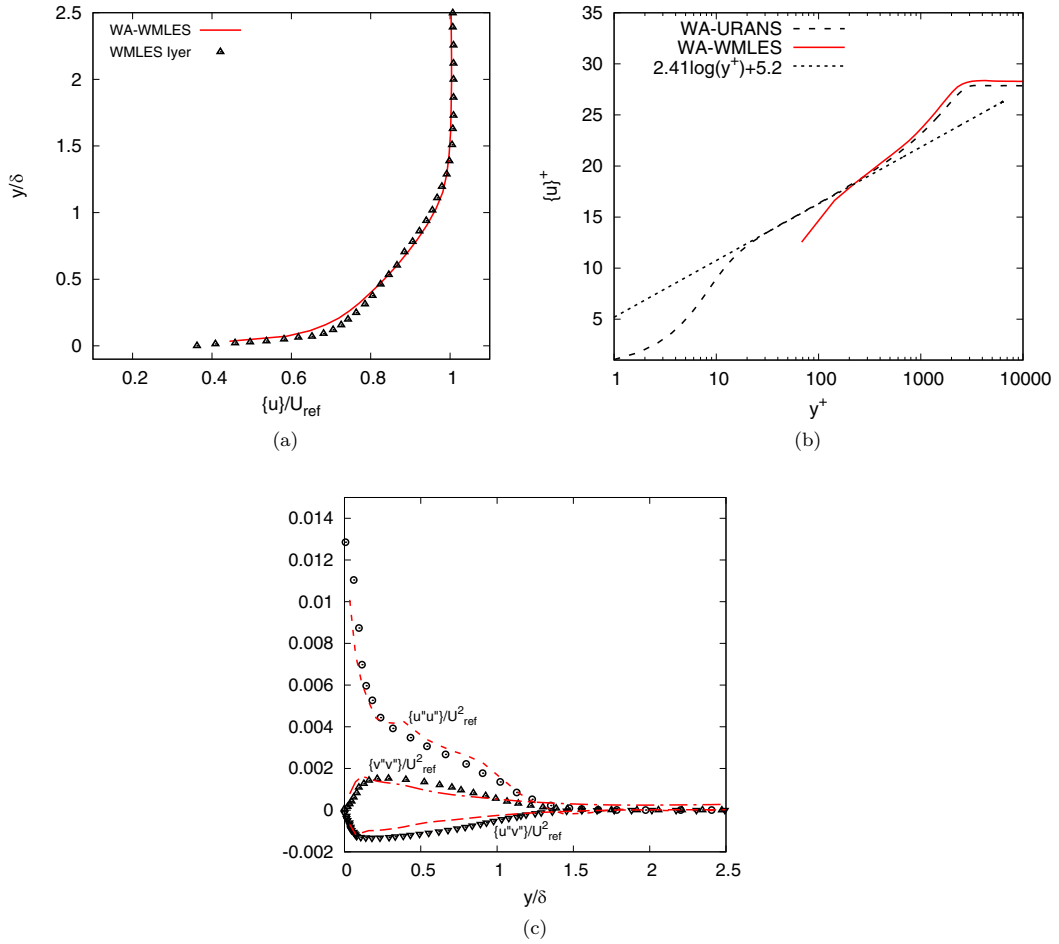

FIG. 7. The mean velocity profile and the turbulence statistics at a streamwise location $x/\delta = 24$ downstream of the inlet. Comparisons are made with the results of the inflow flat plate turbulent boundary layer in Ref. [40]. (a) Time and spanwise averaged streamwise velocity. (b) Time and spanwise averaged streamwise velocity in wall units. (c) Time and spanwise averaged turbulence statistics. Symbols denote the data reported in Ref. [40], while lines denote the results of the current WA-WMLES method.

of the streamwise velocity between these two is depicted in Fig. 8. The sensitivity of the inflow velocity profile has been discussed in Ref. [48], showing that its effect is minimal. In addition, velocity fluctuations obtained from the STG approach are imposed at the inflow plane.

The top wall follows the special profile modeled as an inviscid slip wall. The Euler equations are integrated at the top wall, where the no-penetration condition is explicitly imposed. The pressure and density are corrected based on the pressure balance of the centrifugal force and constant entropy condition, i.e.,

$$\frac{\partial p}{\partial \mathbf{n}} = \kappa \rho |u_\tau|^2, \tag{20}$$

$$\frac{p}{\rho^\gamma} = \frac{p_\infty}{\rho_\infty^\gamma}, \tag{21}$$

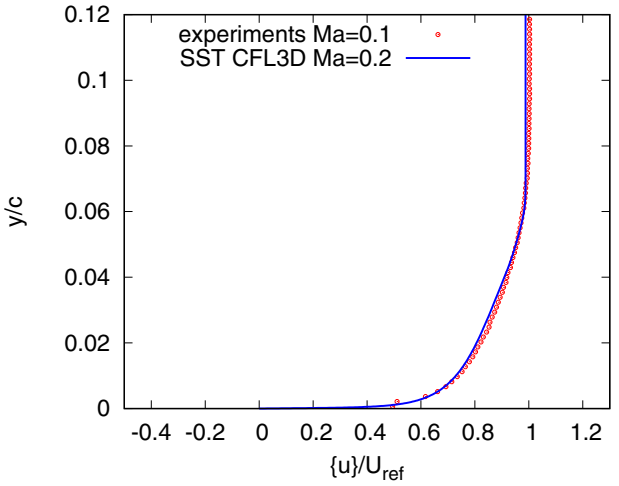

FIG. 8. Time and spanwise averaged streamwise velocity profile at the inflow plane $x/c = -2.14$ for the hump flow compared with the RANS data from the k-ω SST model-based RANS computation using CFL3D.

where $\frac{\partial p}{\partial \mathbf{n}} = \frac{\partial p}{\partial x_j} n_j$ is the pressure gradient with respect to the inward normal direction pointing into the fluid, κ is the signed local curvature, u_τ is the tangential velocity at the inviscid wall, and p_∞ and ρ_∞ are the reference upstream pressure and density, respectively. In terms of numerical implementation, the finite difference form of Eq. (20) and algebraic equation Eq. (21) are solved together iteratively for pressure and density at a local slip-wall mesh point. To suppress the acoustic resonance between the top and bottom walls, as discussed in Ref. [48], a Freund's damping term with the time-averaged pressure as the target pressure is applied in the vicinity of the top wall. Prior to the time-average pressure converges to a relatively smooth field, the RANS initial condition is used as the target pressure field.

At the bottom wall, a nonadaptive mesh on level $j = 6$ with two layers of mesh cells adjacent to the wall is used as discussed in Sec. III B. The finest level is $J = 7$ and further details about the mesh resolution are discussed below. The height of the exchange layer is chosen following the same principle as mentioned in Sec. IV A and is located at the wall-normal distance $d/c = 3.27 \times 10^{-3}$ close to the fourth point from the wall mesh point at $j = 6$. At the inlet, this height corresponds to $y^+ \approx 100$ with the inflow boundary layer thickness $\delta/c = 0.062$. Again, this complies with the suggestion in Ref. [15] to locate the EL below 10% of the boundary layer and that at least three LES cells below the EL are required to prevention from using the under-resolved LES solution that is highly contaminated by numerical and modeling errors as the wall-model input. This height is also close to what is chosen in Refs. [40,50]. The wall boundary conditions are imposed as described in Sec. III B.

The underlying base (coarsest level) mesh size is $60 \times 4 \times 4$ in the streemwise, vertical, and spanwise directions and the finest allowed level of resolution is $J = 7$. Therefore the effective dyadic nested wavelet collocation mesh consists of $3840 \times 256 \times 256 \approx 252$ million points at the finest level of resolution. Hyperbolic tangent distributions in vertical direction are used for mesh clustering in the vicinity of the bottom and top walls. The former is aimed to resolve the boundary layer above the LES-RANS exchange layer while the latter is to resolve the shape of the top-wall profile with large curvature. In the streamwise direction, a mild mesh clustering is also made around the separation point while relatively large mesh spacings are set at the inflow and outflow regions using different coefficients in the hyperbolic tangent functions.

The mesh spacings at the finest level in wall and chord units are summarized in Table III along with corresponding mesh information for selected simulations in the literature. Note that

TABLE III. Grid information used for the hump flow simulations. Both wall and chord units are listed. The wall unit is normalised by the kinematic viscosity over the friction velocity. All wall unit numbers in this table are evaluated at the inflow flat-plate turbulent boundary layer. The subscript "1" denotes the first wall-normal mesh spacing.

Grid	WA-WMLES	WMLES [49]	WMLES [50]	WMLES [40]	WRLES [48]
Δx^+	90	600	300	360	25
$\Delta x/c$	$(3.8 \sim 38)\times10^{-4}$	$(12 \sim 180)\times10^{-4}$	$(12 \sim 200)\times10^{-4}$	$(15 \sim 100)\times10^{-4}$	7.2×10^{-4}
Δz^+	40	100	120	180	12.5
$\Delta z/c$	1.2×10^{-3}	3.1×10^{-3}	3.8×10^{-3}	5.0×10^{-3}	3.6×10^{-4}
Δy_1^+	13	20	50	36	0.8
$\Delta y_1/c$	3.6×10^{-4}	5.5×10^{-4}	13×10^{-4}	$(2.0 \sim 33) \times10^{-4}$	2.2×10^{-5}
Span size/c	0.3	0.4	0.6	0.3	0.4
Total size/million	7.5	9.4	12.9	11	420

the finest effective mesh resolution of the WA-WMLES is consistently smaller than the one used in nonadaptive WMLES, but relatively close to the WRLES, while the similar accuracy is achieved with considerably fewer degrees of freedom than in nonadaptive WMLES. The combination of small mesh size with aggressive compression ratio and effective fine mesh spacing with controlled error are the key attractive points of the WA-WMLES.

As discussed in the previous section different levels of wavelet threshold ϵ are used in the inviscid and viscous regions, whose sizes are estimated by the boundary layer thickness and the size of the separation bubble. The relative threshold values used for adaptation of the momentum, temperature and pressure variables in different regions are summarized in Table IV. Note that as in previous section in addition to adapting on flow variables the mesh is also adapted on the physical coordinates with uniform $\epsilon = 0.005$ and chord length c as an absolute threshold to resolve the geometry and the curvilinear Jacobian. The size of the resulting adaptive mesh based on the above mentioned variable threshold configuration is around 7.5 million with a compression ratio of 97%. It should be noted that the values of ϵ used in WA-WMLES are conservatively smaller compared to a typical range of [0.01,0.1] used in WA-WRLES [2,6]. Numerical experiments demonstrate that the reduction of ϵ for the pressure in the inviscid zone leads to better resolution of the acoustic waves and fewer mesh points compared to larger values of the threshold that result in finer meshes due to contamination of the solution by unphysical disturbances.

2. Simulation results

The adaptive mesh refinement over the separation region is presented in Fig. 9, where the adaptive mesh colored by the levels of resolution is shown. As can be seen from the figure, the mesh resolution throughout most of the boundary layer corresponds to levels $j = 5$ and $j = 6$ with significant adaptive mesh refinement in the separation shear layer region. The flow structure is shown in Fig. 10, where the Q-criterion isosurface colored by the instantaneous streamwise momentum is displayed. Along the front of the hump, stream-wise streaky and small scale vortices are observed, while downstream the hump, larger scale horse-shoe shape vortices are present indicating the strong-intensity turbulent shear layer over the separation recirculation region.

TABLE IV. Wavelet thresholds ϵ used in different variables for the hump flow.

Zone	Momentum	Energy	Pressure	Physical coordinates
Inviscid	0.01	0.01	0.001	0.005
Viscous	0.05	0.05	0.005	0.005

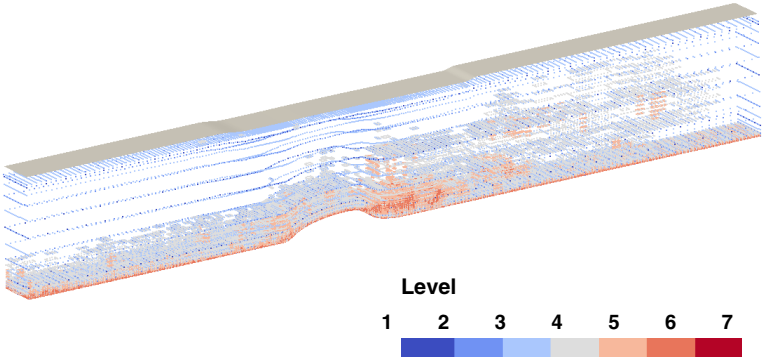

FIG. 9. The adaptive mesh of the WA-WMLES computation colored with levels of resolution for the hump flow.

The effect of the wall model is demonstrated in Fig. 11, where the contours of the instantaneous skin friction coefficient C_f, calculated from the wall shear stress returned from the wall model, are plotted on the streamwise and spanwise plane. Note that in the region of flat plate boundary layer the reasonably high skin friction due to streamwise streak structures is properly predicted by the RANS model. It should be emphasized that without the wall model the viscous flux would be underestimated by the under-resolved WA-LES mesh employed near the wall. The separation region can be identified by the negative dominant values of C_f with subsequent growth of the skin friction coefficient with the resolved fluctuations after the flow reattachment.

The instantaneous field of the streamwise momentum on a streamwise and vertical plane is presented in Fig. 12. In addition to the flow over the bottom slip wall and the separation region, the local flow acceleration and deceleration on the contracted and then expanded top wall are also resolved well by the inviscid boundary condition Eq. (21) using the wavelet-based adaptive finite difference scheme with anisotropic adaptive body-fitted mesh.

The time average is performed after 5 chords flow-through times from the RANS initial condition and accumulates for 10 chords flow-through times. The spanwise averaged statistics are computed by interpolating the continuous wavelet basis onto 2D, nonadaptive sampling mesh at level $j = 5$ and averaging across multiple slices in the streamwise and vertical plane. The time and spanwise averaged pressure and streamwise momentum contours are plotted in Figs. 13 and 14. Due to the relatively low Mach number, the pressure deviation from the free-stream reference value is

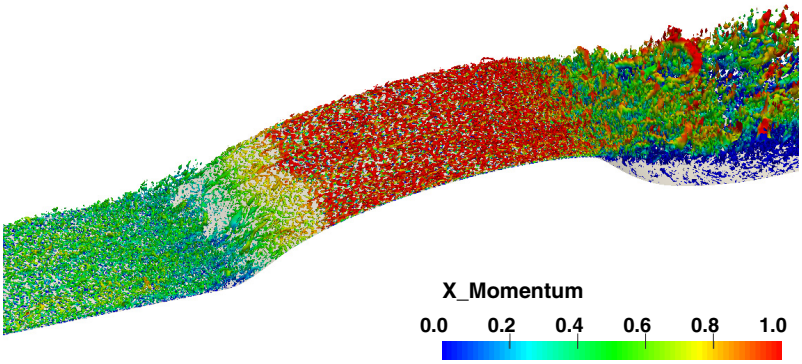

FIG. 10. The instantaneous Q-criterion isosurface colored by instantaneous streamwise momentum for the hump flow.

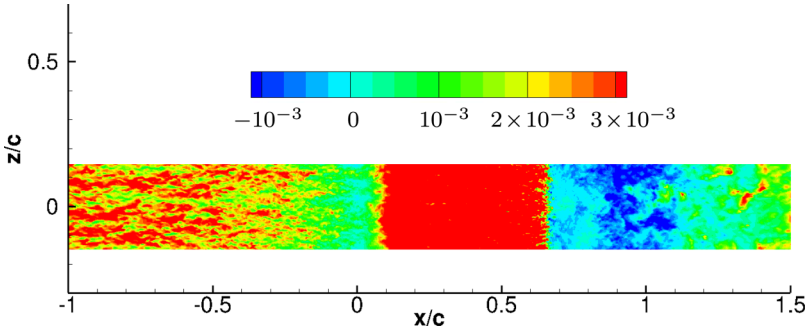

FIG. 11. The instantaneous skin friction coefficient on the streamwise and spanwise plane for the hump flow.

much smaller than that of the momentum, which implies the need of using relatively small wavelet threshold for better resolution of the pressure field, especially in the inviscid region.

The time and spanwise averaged skin friction and pressure coefficients over the wall are, respectively, plotted in Figs. 15(a) and 15(b), where the WRLES data [48], nonadaptive WMLES results [40,50], the CFL3D results of $k-\omega$ SST RANS model used as the initial condition for WA-WMLES, and the experimental data [43] are plotted for comparison. Note that all WMLES results are obtained with the same equilibrium wall model Eq. (11). As seen in Fig. 15(a), the upstream C_f is slightly low for the current simulation because the applied RANS inflow velocity profile from the CFL3D calculation has slightly lower momentum. Nevertheless, the upstream C_f for the WA-WMLES is very close to the results of RANS computation, which validates the WA-WMLES method along with the synthetic turbulence generator for the inflow boundary conditions and RANS velocity inflow profile. In the flow acceleration region, only the WRLES results agree well with the experimental C_f. The skin friction coefficient curves over the hump surface are close for all WA-WMLES and nonadaptive WMLES, but differ from the other three sets of data. In the region after reattachment, the WA-WMLES C_f deviates from the nonadaptive WMLES reference results and gets close to the RANS, which is consistent with the inflow RANS velocity profile with slightly lower momentum than the other reference data. As to the surface pressure distribution shown in Fig. 15(b), all cases are very close to each other upstream the half way of the hump front and deviate from each other after that. Overall the WA-WMLES and both WMLES results for pressure coefficient are close to each other and the discrepancies among all cases are smaller than those of the C_f results.

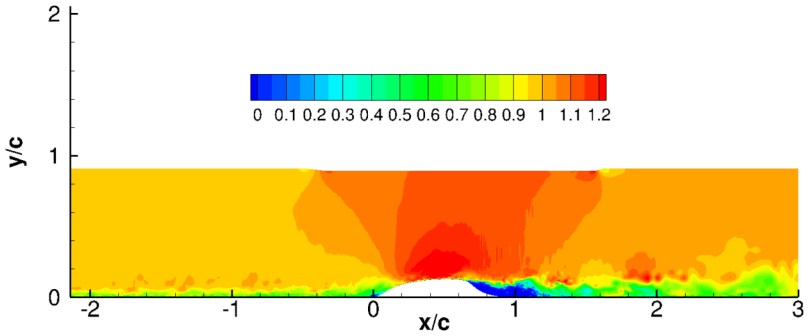

FIG. 12. The instantaneous streamwise momentum on the streamwise and wall normal plane for the hump flow.

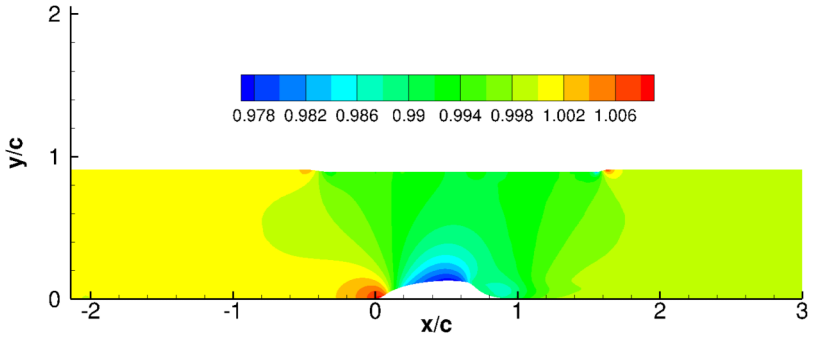

FIG. 13. The time and spanwise averaged pressure on the streamwise and wall normal plane for the hump flow.

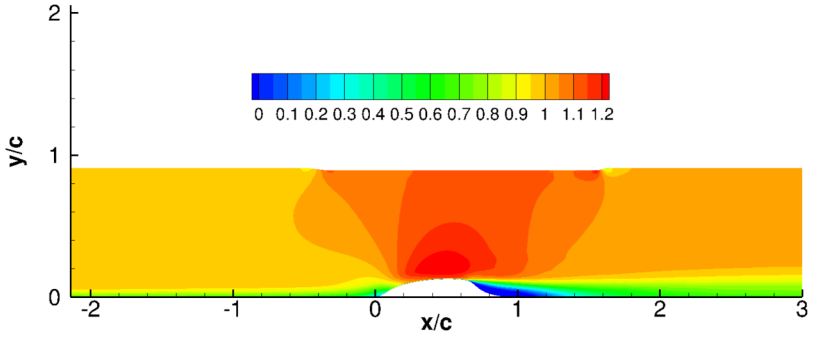

FIG. 14. The time and spanwise averaged streamwise momentum on the streamwise and wall normal plane for the hump flow.

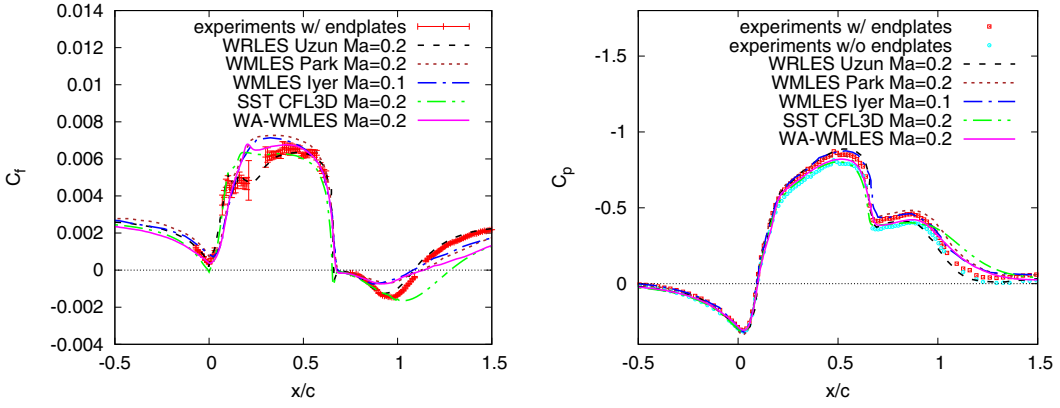

FIG. 15. Time and spanwise averaged skin friction and pressure coefficients over the wall for the hump flow. Comparisons are made with the wall-resolved LES data [48], nonadaptive WMLES results [40,50], the RANS data using the k-ω SST model by CFL3D, i.e., the initial condition of WA-WMLES, and the experimental data [43]. (a) Skin friction coefficient C_f. (b) Pressure coefficient C_p.

TABLE V. Comparison of separation and reattachment locations. Note that all WMLES cases use the equilibrium wall model.

Case	Separation (x/c)	Reattachment (x/c)	Bubble length ($\Delta x/c$)	Error in bubble
WA-WMLES	0.677	1.138	0.461	6.0%
WMLES [50]	0.680	1.084	0.404	−7.1%
WMLES [40]	0.655	1.105	0.450	3.4%
WRLES [48]	0.641	1.09	0.449	3.2%
Experiment [43]	0.665(±0.005)	1.10(±0.005)	0.435	–

The separation and reattachment locations for the current simulation and the reference data are compared in Table V. Note that the listed data of the nonadaptive WMLES results correspond to case "EQWM G2" in Ref. [50] and case "fWM3" in Ref. [40]. The bubble length and the error in bubble length are also compared. Overall the WA-WMLES results are similar to results of the other simulations, especially taking into account that many aspects of numerical simulations may affect the predicted separation bubble. Some factors include but not limited to detailed implementations of the wall-modeled viscous flux boundary conditions, the upstream turbulent boundary layer in terms of momentum thicknesses, treatment of the outflow boundary conditions, and spatial and temporal discretization errors. These factors can hardly be exactly the same depending on the limitation of each solver.

The time and spanwise averaged streamwise velocity profiles $\{u\}$ at $x/c = -0.81$ are plotted in Fig. 16. This location is a proper station to compare the solution of upstream turbulent boundary layer flow. The mean velocity agrees well with the nonadaptive WMLES result [40] as shown in Fig. 16(a). In Fig. 16(b), the same profile in wall unites is compared with the RANS data using the k-ω SST model by CFL3D. This good agreement shows that the WA-WMLES resolves the fully developed turbulent boundary layer. Note that the y^+ value at the crossing point between the WA-WMLES and the log-law profiles is the exchange location of the WA-LES solution with the equilibrium wall-model computation.

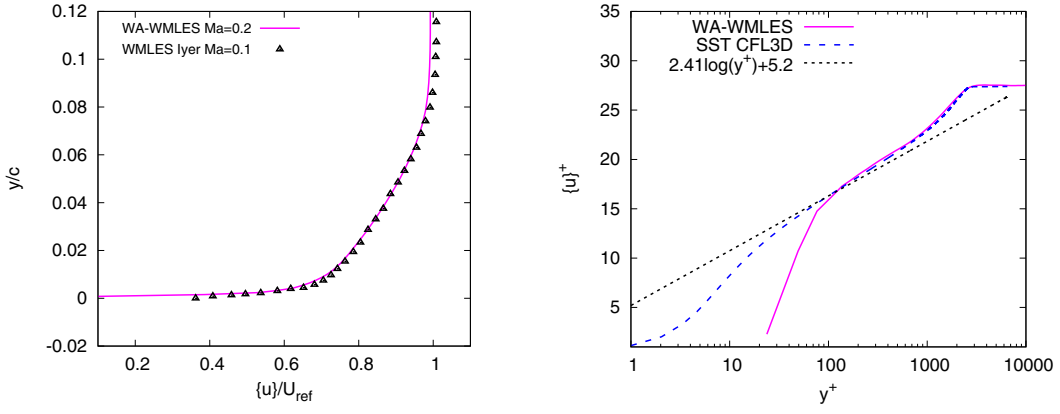

FIG. 16. Time and spanwise averaged streamwise velocity profile at $x/c = -0.81$ for the hump flow compared with the nonadaptive WMLES case [40] (a) and the velocity profile, scaled by wall units, compared with the RANS data using the k-ω SST model by CFL3D(b). (a) Velocity profile scaled by the free-stream velocity. (b) Velocity profile scaled by the wall units.

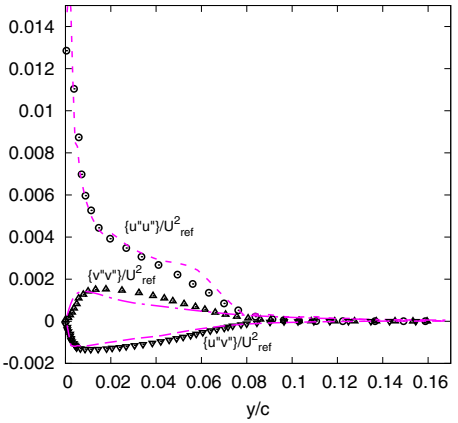

FIG. 17. Time and spanwise averaged profiles (lines) of turbulence fluctuation statistics at $x/c = -0.81$ for the hump flow compared with the nonadaptive WMLES case [40] (symbols).

Similarly, the time and spanwise averaged turbulent stress profiles $\{u''u''\}$, $\{v''v''\}$, and $\{u''v''\}$ at the same location are shown in Fig. 17. The slight differences between the present WA-WMLES and nonadaptive WMLES [40] may attribute to different effective mesh resolution applied in the two methods, the error introduced by the wavelet filtering threshold as well as other different flow configurations such as the free-stream Mach number (0.2 versus 0.1) and inflow turbulence

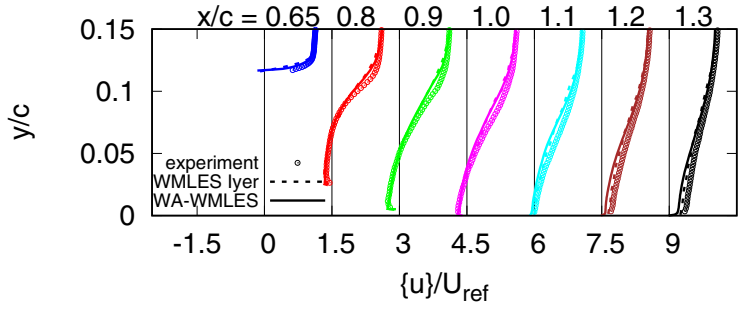

(a)

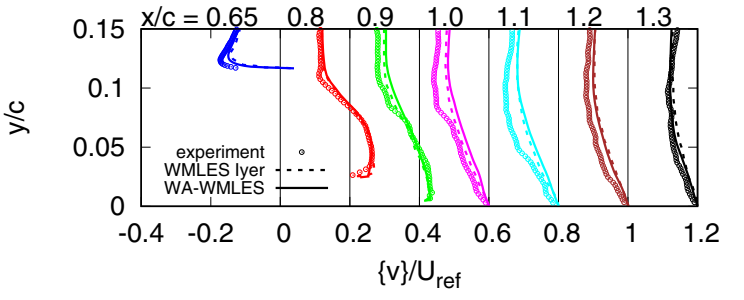

(b)

FIG. 18. Time and spanwise averaged velocity profiles at different streamwise locations. The experimental data [43] and those of the nonadaptive WMLES [40] are shown for comparison. (a) Streamwise velocity. (b) Vertical velocity.

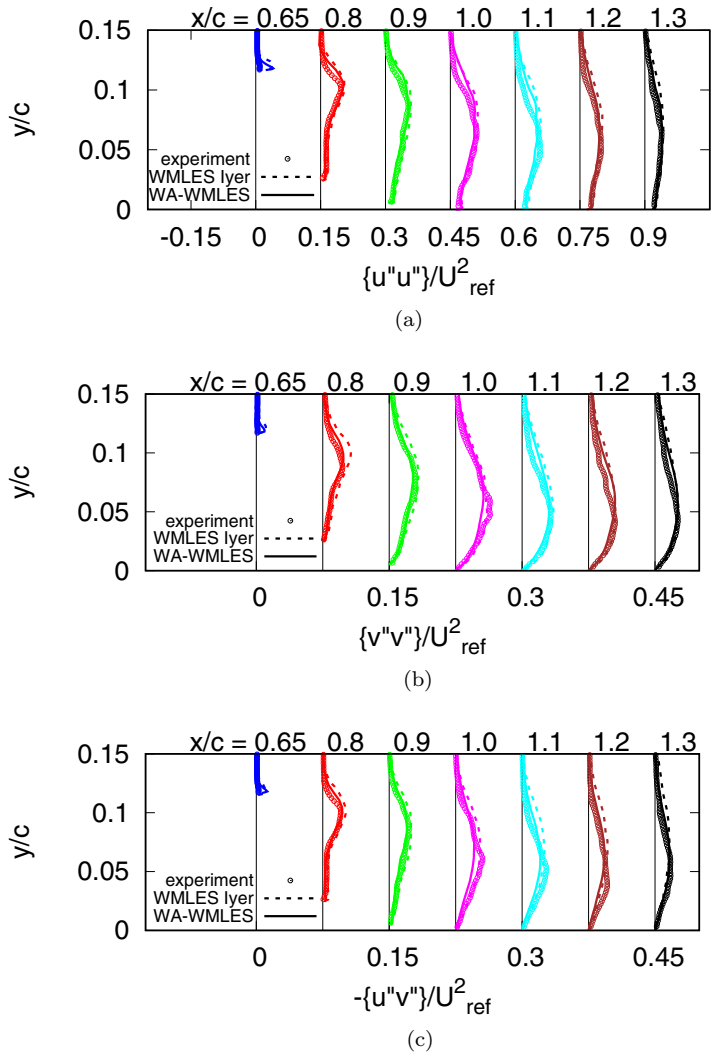

FIG. 19. Time and spanwise averaged turbulent stress profiles at different streamwise locations. The experimental data [43] and those of the nonadaptive WMLES [40] are shown for comparison. (a) $\{u''u''\}$, (b) $\{v''v''\}$, and (c) $\{u''v''\}$.

generation techniques (Fourier modes method versus digital filtering method). As already discussed in Sec. IV A, the zonal wavelet thresholds cause an artificial plateau in $\{u''u''\}$ around the edge of the boundary layer, as observed in Fig. 17.

The time and spanwise averaged velocity profiles in the streamwise (a) and vertical (b) directions at multiple streamwise stations are shown Fig. 18. These stations are chosen upstream from the separation location downstream to the reattachment region mainly due to poor predictions of the RANS computations [44] in this part of the flow. The present WA-WMLES results are in satisfactory agreement with the experimental data. Slightly larger discrepancies for the vertical velocity profile are observed at stations between $x/c = 0.9$ and $x/c = 1.1$ are also generally seen in other nonadaptive WMLES simulations [40,50]. One explanation for the larger discrepancies in the vertical velocity for the WA-WMLES is that the grid adaptation based on the momentum is actually performed based on the momentum magnitude instead of independently for each component.

Considering the vertical velocity is one order of magnitude smaller than the stream-wise velocity, the relative errors controlled by the wavelet threshold result in a larger absolute vertical component error.

The turbulent stress profiles $\{u''u''\}$, $\{v''v''\}$, and $\{u''v''\}$ at different stations are plotted in Fig. 19. All results agree fairly well with the experimental data except those with over-prediction at $x/c = 0.65$, where the turbulence stress values are relatively small. This is also observed in other nonadaptive WMLES simulations [40,50]. As seen in Fig. 19 the turbulent stresses at the other considered stations in general are in closer agreement with the experimental data than the nonadaptive equilibrium WMLES results of case "fWM3" in Ref. [40]. Overall, the performance of the WA-WMLES method with the equilibrium wall model for this particular challenging separated flow problem is satisfactory, especially taking into account the relatively small number of adaptive mesh points despite fairly fine effective mesh resolution as summarized in Table III.

V. CONCLUSIONS

A wavelet-based adaptive wall-modeled large eddy simulation method is proposed for simulations of wall-bounded compressible turbulent flows. The approach utilizes the wavelet-based adaptive large eddy simulation, incorporated into the anisotropic-adaptive wavelet collocation method, to resolve the outer region of turbulent boundary layer, while the inner part is approximated by the wall-shear-stress model. For the first time, the WA-WMLES method extends the application of the wavelet-based adaptive method to a realistic wall-bounded turbulent flow configuration at a relatively high (order of a million) Reynolds number based on the length scale of the body shape. Previously reported wavelet-based methods, such as WA-LES and WA-DDES, would have required substantially larger computational resources to solve the same problem. The WA-WMLES method with the considered equilibrium wall model performs fairly well for wall-bounded flows with zero, mild (with flow deceleration), and moderate (with shape induced flow separation) pressure gradients, as demonstrated by the two test cases: the flat plate turbulent boundary layer flow and the separated flow over the NASA wall-mounted hump. The combination of small mesh size with aggressive compression ratio, the effective fine mesh spacing with controlled error through carefully chosen wavelet filtering threshold, and ability to reliably predict turbulent flow characteristics for practically challenging problems are attractive features of the WA-WMLES method. Further development of WA-WMLES may include the use of variable threshold ϵ that depends on the solution, e.g., the vorticity field, and identifies the inviscid and viscous flow regions. Finally, to improve the performance of the WA-WMLES method for problems with strong pressure gradients (e.g., shock wave induced separation) the approach needs to be extended to the nonequilibrium wall model.

ACKNOWLEDGMENTS

X.G. and M.Y.H. were supported by NASA's Transformational Tools and Technologies (TTT) Project Grant No. NNX15AU24A and NIA Subaward No. 201151-FSU. The authors are thankful for the computing time on the Extreme Science and Engineering Discovery Environment (XSEDE) supported by National Science Foundation Grant No. ACI-1548562, as well as the RCC HPC system at Florida State University.

[1] G. De Stefano and O. V. Vasilyev, A fully adaptive wavelet-based approach to homogeneous turbulence simulation, J. Fluid Mech. **695**, 149 (2012).

[2] G. De Stefano and O. V. Vasilyev, Wavelet-based adaptive simulations of three-dimensional flow past a square cylinder, J. Fluid Mech. **748**, 433 (2014).

[3] D. E. Goldstein and O. V. Vasilyev, Stochastic coherent adaptive large eddy simulation method, Phys. Fluids **16**, 2497 (2004).

[4] G. De Stefano, D. E. Goldstein, and O. V. Vasilyev, On the role of subgrid-scale coherent modes in large-eddy simulation, J. Fluid Mech. **525**, 263 (2005).
[5] G. De Stefano, A. Nejadmalayeri, and O. V. Vasilyev, Wall-resolved wavelet-based adaptive large-eddy simulation of bluff-body flows with variable thresholding, J. Fluid Mech. **788**, 303 (2016).
[6] G. De Stefano, E. Brown-Dymkoski, and O. V. Vasilyev, Wavelet-based adaptive large-eddy simulation of supersonic channel flow, J. Fluid Mech. **901**, A13 (2020).
[7] E. Brown-Dymkoski and O. V. Vasilyev, Adaptive-anisotropic wavelet collocation method on general curvilinear coordinate systems, J. Comput. Phys. **333**, 414 (2017).
[8] A. Nejadmalayeri, A. Vezolainen, E. Brown-Dymkoski, and O. V. Vasilyev, Parallel adaptive wavelet collocation method for PDEs, J. Comput. Phys. **298**, 237 (2015).
[9] O. V. Vasilyev, Solving multidimensional evolution problems with localized structures using second generation wavelets, Int. J. Comput. Fluid Dynam. **17**, 151 (2003).
[10] O. V. Vasilyev and C. Bowman, Second-generation wavelet collocation method for the solution of partial differential equations, J. Comput. Phys. **165**, 660 (2000).
[11] O. V. Vasilyev and N. K.-R. Kevlahan, An adaptive multilevel wavelet collocation method for elliptic problems, J. Comput. Phys. **206**, 412 (2005).
[12] H. Choi and P. Moin, Grid-point requirements for large eddy simulation: Chapman's estimates revisited, Phys. Fluids **24**, 011702 (2012).
[13] J. Larsson, S. Kawai, J. Bodart, and I. Bermejo-Moreno, Large eddy simulation with modeled wall-stress: Recent progress and future directions, Mech. Eng. Rev. **3**, 15-00418 (2016).
[14] P. R. Spalart, Detached-eddy simulation, Annu. Rev. Fluid Mech. **41**, 181 (2009).
[15] S. Kawai and J. Larsson, Wall-modeling in large eddy simulation: Length scales, grid resolution, and accuracy, Phys. Fluids **24**, 015105 (2012).
[16] M. L. Shur, P. R. Spalart, M. Kh. Strelets, and A. K. Travin, A hybrid RANS-LES approach with delayed-DES and wall-modelled LES capabilities, Int. J. Heat Fluid Flow **29**, 1638 (2008).
[17] P. R. Spalart, S. Deck, M. L. Shur, K. D. Squires, M. Kh. Strelets, and A. Travin, A new version of detached-eddy simulation, resistant to ambiguous grid densities, Theor. Comput. Fluid Dyn. **20**, 181 (2006).
[18] J. Larsson, F. S. Lien, and E. Yee, Feedback-controlled forcing in hybrid LES-RANS, Int. J. Comput. Fluid Dynam. **20**, 687 (2006).
[19] M. Shur, P. R. Spalart, M. Strelets, and A. Travin, Detached-eddy simulation of an airfoil at high angle of attack, Eng. Turbul. Model. Exp. **4**, 669 (1999).
[20] E. Balaras, C. Benocci, and U. Piomelli, Two-layer approximate boundary conditions for large-eddy simulations, AIAA J. **34**, 1111 (1996).
[21] W. Cabot and P. Moin, Approximate wall boundary conditions in the large-eddy simulation of high Reynolds number flow, Flow, Turbul. Combust. **63**, 269 (2000).
[22] S. Kawai and J. Larsson, Dynamic nonequilibrium wall-modeling for large eddy simulation at high Reynolds numbers, Phys. Fluids **25**, 015105 (2013).
[23] G. I. Park and P. Moin, An improved dynamic nonequilibrium wall-model for large eddy simulation, Phys. Fluids **26**, 015108 (2014).
[24] Xuan Ge, O. Vasilyev, and M. Yousuff Hussaini, Wavelet-based adaptive delayed detached eddy simulations for wall-bounded compressible turbulent flows, J. Fluid Mech. **873**, 1116 (2019).
[25] X. Ge, Y. Zhou, O. V. Vasilyev, and M. Y. Hussaini, Adaptive wavelet-based delayed detached eddy simulations of anisothermal channel flows with high transverse temperature gradients, in *Proceedings of the AIAA Scitech Forum* (AIAA, Reston, VA, 2019), p. 1558.
[26] Xuan Ge, O. V. Vasilyev, G. De Stefano, and M. Y. Hussaini, Wavelet-based adaptive unsteady reynolds-averaged navier-stokes computations of wall-bounded internal and external compressible turbulent flows, in *Proceedings of the AIAA Aerospace Sciences Meeting* (AIAA, Reston, VA, 2018), p. 0545.
[27] X. Ge, O. V. Vasilyev, G. De Stefano, and M. Yousuff Hussaini, Wavelet-based adaptive unsteady Reynolds-averaged Navier-Stokes simulations of wall-bounded compressible turbulent flows, AIAA J. **58**, 1529 (2020).

[28] J. Bodart and J. Larsson, Wall-Modeled Large Eddy Simulation in Complex Geometries with Application to High-Lift Devices, *Annual Research Briefs, Center for Turbulence Research, Stanford University* (2012), pp. 37–48.
[29] J. Bodart, J. Larsson, and P. Moin, Large eddy simulation of high-lift devices, in *Proceedings of the 21st AIAA Computational Fluid Dynamics Conference* (AIAA, San Diego, CA, 2013), p. 2724.
[30] W. Rozema, H. J. Bae, P. Moin, and R. Verstappen, Minimum-dissipation models for large-eddy simulation, Phys. Fluids **27**, 085107 (2015).
[31] R. Verstappen, When does eddy viscosity damp subfilter scales sufficiently? J. Sci. Comput. **49**, 94 (2011).
[32] A. Nejadmalayeri, A. Vezolainen, and O. V. Vasilyev, Reynolds number scaling of coherent vortex simulation and stochastic coherent adaptive large eddy simulation, Phys. Fluids **25**, 110823 (2013).
[33] D. L. Donoho, Interpolating wavelet transforms, Technical Report 408, Department of Statistics, Stanford University (1992), https://statistics.stanford.edu/research/interpolating-wavelet-transforms.
[34] K. Devine, E. Boman, R. Heaphy, B. Hendrickson, and C. Vaughan, Zoltan data management services for parallel dynamic applications, Comput. Sci. Eng. **4**, 90 (2002).
[35] J. B. Freund, Proposed inflow/outflow boundary condition for direct computation of aerodynamic sound, AIAA J. **35**, 740 (1997).
[36] T. J. Poinsot and S. K. Lelef, Boundary conditions for direct simulations of compressible viscous flows, J. Comput. Phys. **101**, 104 (1992).
[37] M. L. Shur, P. R. Spalart, M. K. Strelets, and A. K. Travin, Synthetic turbulence generators for RANS-LES interfaces in zonal simulations of aerodynamic and aeroacoustic problems, Flow, Turbul. Combust. **93**, 63 (2014).
[38] G. Eitel-Amor, R. Örlü, and P. Schlatter, Simulation and validation of a spatially evolving turbulent boundary layer up to $\mathrm{Re}_\theta = 8300$, Int. J. Heat Fluid Flow **47**, 57 (2014).
[39] M. V. Morkovin, Effects of compressibility on turbulent flows, in *Mécanique de la Turbulence*, edited by A. Favre (CNRS, Paris, 1962), pp. 367–380.
[40] P. S. Iyer and M. R. Malik, Wall-modeled large eddy simulation of flow over a wall-mounted hump, in *Proceedings of the 46th AIAA Fluid Dynamics Conference* (AIAA, Reston, VA, 2016), p. 3186.
[41] E. Brown-Dymkoski, Adaptive wavelet-based turbulence modeling for compressible flows in complex geometry, Ph.D. thesis, Department of Mechanical Engineering, University of Colorado at Boulder, 2016.
[42] P. R. Spalart, K. V. Belyaev, A. V. Garbaruk, M. L. Shur, M. Kh. Strelets, and A. K. Travin, Large-eddy and direct numerical simulations of the bachalo-johnson flow with shock-induced separation, Flow Turbulence Combust **99**, 865 (2017).
[43] D. Greenblatt, K. B. Paschal, C.-S. Yao, J. Harris, N. W. Schaeffler, and A. E. Washburn, Experimental investigation of separation control part 1: Baseline and steady suction, AIAA J. **44**, 2820 (2006).
[44] C. L. Rumsey, T. B. Gatski, W. L. Sellers III, V. N. Vasta, and S. A. Viken, Summary of the 2004 computational fluid dynamics validation workshop on synthetic jets, AIAA J. **44**, 194 (2006).
[45] https://turbmodels.larc.nasa.gov/nasahump_grids.html (last accessed on May 31, 2021).
[46] https://turbmodels.larc.nasa.gov/nasahump_val_sst.html (last accessed on May 31, 2021).
[47] https://cfl3d.larc.nasa.gov/ (last accessed May 31, 2021).
[48] A. Uzun and M. R. Malik, Large-eddy simulation of flow over a wall-mounted hump with separation and reattachment, AIAA J. **56**, 715 (2018).
[49] A. Avdis, S. Lardeau, and M. Leschziner, Large eddy simulation of separated flow over a two-dimensional hump with and without control by means of a synthetic slot-jet, Flow Turbul. Combust. **83**, 343 (2009).
[50] G. I. Park, Wall-modeled large-eddy simulation of a high Reynolds number separating and reattaching flow, AIAA J. **55**, 3709 (2017).